The Magnetic Properties of Electrical Pulses Delivered by Deep-Brain Stimulation Systems

Mevlüt Yalaz, Alexander Teplyuk, Muthuraman Muthuraman, Günther Deuschl, and Michael Höft, *Senior Member, IEEE*

***Abstract*— The aim of this article is to analyze the magnetic field properties for both the monopolar and bipolar electrode configurations of deep-brain stimulation electrodes using 3-D magnetic field measurements and to investigate if the magnetic measurements enable a localization of the electrode as a proof of concept. Therefore, a simplified head phantom with an integrated deep-brain stimulation electrode was created to measure the magnetic flux densities in all the three dimensions with a fluxgate magnetometer over a sensor trajectory of measuring points inside the magnetically shielded chamber. The magnitude of the magnetic flux density for monopolar stimulation and bipolar stimulation is in the nT and pT ranges for the frequency 160 Hz, depending on the stimulation amplitude and on the distance between the sensor and the electrode. The field distributions show a linear decline in the magnetic field for the monopolar and a quadratic decline for the bipolar stimulation. We were able to reconstruct the magnetic field using multiple recording sites. As the magnetic field of deep-brain stimulation can be measured and its field strength can be reconstructed, it is feasible to estimate the strength of the field within the limits of programmable stimulation parameters and distance between the sensor and the electrode. The presented results are intended as preliminary work for the further development of electrode localization methods using magnetic measurements. As an example of the feasibility of electrode localization, this article presents a bipolar measurement that creates a more focused spatial field distribution and results in an accurate localization.**

***Index Terms*— Deep-brain stimulation (DBS), fluxgate magnetometer, magnetic field measurement, monopolar bipolar stimulation, neurostimulator.**

I. Introduction

DEEP-brain stimulation (DBS) is an established treatment of movement disorders such as Parkinson's disease (PD), dystonia, or tremors [1]–[3]. The most common targets are the subthalamic nucleus (STN) for PD, the globus pallidus internus (GPi) for dystonia, and the nucleus ventrointermedius internus (Vim) for tremors. During surgery, these targets are determined with stereotactic methods based on the magnetic resonance images (MRIs), which are obtained with a stereotactic ring. The electrodes are connected to the neurostimulator that is surgically placed under the skin near the clavicle, which delivers the DBS signal according to the patients' needs. The amplitude of the stimulation signal is commonly set between 1 and 4 V, the pulsewidth between 60 and 250 μs, the frequency between 130 and 185 Hz, and the stimulation mode between monopolar and bipolar electrode configuration [4]. The stimulation elicits a corresponding spatial distribution of the stimulation field around the electrodes that causes the extent of the neural activation or the volume of tissue activated (VTA). The size of the VTA during DBS is adapted to improve the clinical benefit of DBS [5], [6], considering the tradeoff between minimizing side effects and maximizing clinical improvement. To mathematically model the stimulated field, the exact position of the electrode in the brain must be determined [7], [8]. One neuroimaging approach opportunity is to localize the DBS electrodes via metal artifacts in computed tomography (CT) [9] or postoperative MRI images [10]–[12] or in combination of both [13]. The other way is to locate a single source that is responsible for a certain frequency from the signal by using noninvasive modalities like electroencephalography (EEG) or magnetoencephalography (MEG). Parametric approaches like dipole-fit methods estimating the source that best explains the measured data can be used [14]. In order to have a satisfactory match of the mathematical model with the considered measurement, a mathematical model estimation must be made, which ensures the magnetic field properties analyzed in this article. To diminish the magnetic noise, a magnetically shielded chamber is required during data acquisition [15], [16].

In this article, magnetic field measurements for monopolar and bipolar electrode configurations are performed to investigate its magnetic field properties. This may be of interest for different research areas. First, the magnetic properties of DBS are needed for the development of suitable magnetic sensors that operate at room temperature and outside the shielded chamber, e.g., magnetoelectric sensors [17]. Second, the distortion of the investigated magnetic field distribution can be used to test the safety of the system against electromagnetic fields generated by various electrical devices. A first

This work was supported by the German Research Foundation (Deutsche Forschungsgemeinschaft, DFG) through the Project B5 and Z2 of the Collaborative Research Centre CRC 1261 *Magnetoelectric Sensors: From Composite Materials to Biomagnetic Diagnostics*. The Associate Editor coordinating the review process was Seyed Hossein Sadeghi. *(Corresponding author: Mevlüt Yalaz).*

M. Yalaz, A. Teplyuk, and M. Höft are with the Chair of Microwave Engineering, Christian Albrecht's University, 24143 Kiel, Germany (e-mail: my@tf.uni-kiel.de; alt@tf.uni-kiel.de; mh@tf.uni-kiel.de).

M. Muthuraman is with the Department of Neurology, Johannes Gutenberg University, 55131 Mainz, Germany (e-mail: m.muthura@uni-mainz.de).

G. Deuschl is with the Department of Neurology, Christian Albrecht's University, 24105 Kiel, Germany (e-mail: g.deuschl@neurologie.uni-kiel.de).

experimental study has been published [18]. Furthermore, by knowing the distribution of the magnetic field strength at the scalp level through the invasive DBS system, an estimation of how strong and in which direction the magnetic field might be stimulated in noninvasive brain stimulation technologies such as transcranial magnetic stimulation (TMS) [19], transcranial direct current stimulation (tDCS) [20], or magnetic field projector (MFP) [21] can be given.

We are mainly interested in locating the DBS electrode with magnetic field measurements. This is intended to be an alternative to conventional magnetic resonance imaging techniques as described above that are affected by metal artifacts causing errors of up to 10.4 mm [22]. Significant discrepancies have also been reported between the electrode centers estimating by CT and MRI. On the other hand, microelectrode recording (MER) during surgery is used to confirm the target location by recording the discharge patterns of single neurons that identify the interested brain structures (i.e., STN, GPi, and Vim). Retrospective analysis of the tracking error of the microelectrode was performed between the planned trajectory and the microelectrode tip, giving a total error of 1.2 mm [23]. Nevertheless, MER is time-consuming and requires the patient to be awake. From a clinical perspective, identifying the exact target area within the brain is still not yet precisely defined. The exact determination of the target area, therefore, plays an important role in achieving optimal clinical results. Electrode localization has also been tried as a proof of concept with EEG recordings on the scalp [24]; however, this article deals with the magnetic side of DBS. Future perspectives include to identify the best contact of the electrode for reaching the anatomically defined stimulation target area in the brain.

II. Methods

A. Head Phantom

A simplified phantom head with the shape of a cylinder as shown in Fig. 1(a) with dimensions comparable with a human head, as shown in Fig. 1(b), was developed to model the measurement of the magnetic field, and was filled with an isotonic fluid (NaCl 0.9 %) to mimic the electric conductivity of a human brain. The cylinder body is made of acrylic glass and, therefore, is neither electrically conductive nor magnetic. The electrode can be moved in the x- and y-directions by rotating the adjustment wheel [see Figs. 1(a) and 2], and in the z-direction by pulling up and down the electrode holder and can, thereby, be placed at any fixed position. Thus, it is possible to measure the exact stereotactic position of the electrode, which ensures the accuracy of this model.

B. Stimulation System

The used Medtronic 3387 DBS electrode, as shown in Fig. 3, consists of a polyurethane outer jacket and has a diameter of 1.27 mm and four independent annular platinum–iridium contacts with 1.5 mm in length and 1.5 mm apart from each other. Two types of stimulation modes are applied, which differ in electrical polarity. In the case of bipolar stimulation, two contacts of the electrode are activated, one as the cathode

(a)

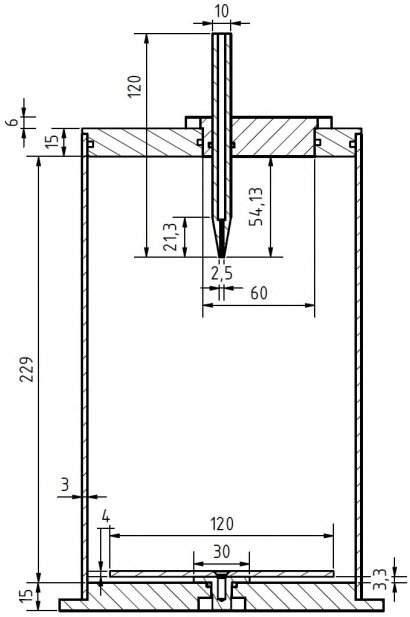

(b)

Fig. 1. Top: Cylindrical phantom head and the fluxgate sensor with its all three orthogonal measuring directions that are used for the measurements. The rotation point of the sensor is also the assumed measuring point. Bottom: Dimensions of this phantom in millimeter.

(negative pole) and another one as the anode (positive pole), whereas in monopolar stimulation, one of the contacts is programed as the cathode, while the neurostimulator is used as the anode [25], [26]. Since the stimulator could not be placed in the cylinder easily, a round nonmagnetic titanium plate at the bottom of the cylinder is added that represents the neurostimulator as the anode in the case of monopolar electrode configuration.

C. Recording System

To measure the magnetoelectrical properties, the whole recordings took place in a magnetically shielded measuring

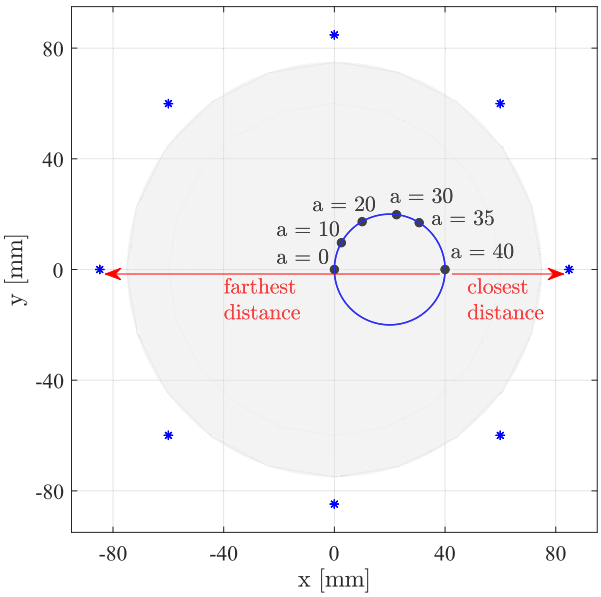

Fig. 2. Top view of the cylinder with the radius of 75 mm (gray circular area). The electrode can be rotated along the inner circle (blue). The distance to the origin defines the variable a, which can be set between $a = 0$ mm and $a = 40$ mm with the corresponding xy coordinates. Blue asterisk markers: positions of the measuring points. Red arrows: closest (45 mm) and farthest (125 mm) measuring points to the position $a = 40$ mm.

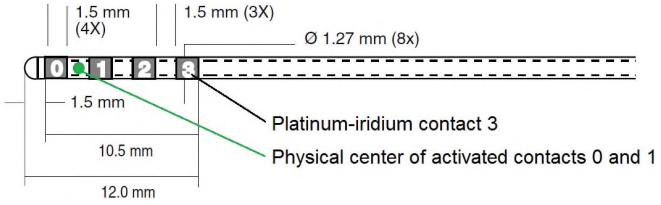

Fig. 3. Dimensions of the Medtronic Model 3387 DBS Electrode [27]. As an example, the physical center point of the bipolar electrode configuration with activated contacts 0 and 1 is marked as a green dot marker.

chamber (Series Ak3B, Vacuumschmelze GmbH). The head scanner inside the chamber was constructed in-house with non-ferromagnetic materials and operates pneumatically to avoid interfering electromagnetic fields due to electrically driven stepping motors. The entire electronic equipment to drive the scanner is located outside the chamber. With this head scanner, an optimized sensor trajectory of variable measuring points around the head phantom with the desired spatial resolution can be programed.

The attached unidirectional fluxgate magnetometer (Fluxmaster, Stefan Mayer Instruments) is oriented at each measuring point in all three orthogonal directions to get the complete magnetic information at this point by rotation of its sensitive axis, as shown in Fig. 1(a). The rotational axis (red-dashed line) is aligned to the diagonal axis of the three orthogonal sensing axes [i.e., along vector (1,1,1)']. At first, the first magnetic field component B_1 is measured in direction 1 [vector (1,0,0)'], then direction 2 [vector (0,1,0)'] is obtained by $+120°$ rotation of the sensor around the rotation axis by proper mechanical mean driven by air pressure and the second field component B_2 is measured. Finally, the same procedure is performed with direction 3 [vector (0,0,1)'], by further 120° rotation to measure the third field component B_3. This is necessary for calculating the magnitude of the magnetic flux density with $(B_1^2 + B_2^2 + B_3^2)^{1/2}$. Since the sensor has a diameter of 10 mm and a length of 30 mm, it is fixed that the point exactly in the middle of the detection coil with a length of 20 mm placed in the front of the sensor represents the measuring point and is, thus, the rotating point of the sensor. The red point marker in Fig. 1(a) represents the measuring point that has a distance of 11 mm (half of the detection coil length 10 mm plus protective cover of 1 mm) to the front of the sensor. It has a noise level of typically 20 $\mathrm{pT/(Hz)^{1/2}}$ at 1 Hz and a bandwidth of 1 kHz from 0 to 1 kHz. The recorded signals of the fluxgate sensor were amplified with a low-noise preamplifier (Model SR560, Stanford Research Systems) by a factor of 10 for monopolar and 1000 for bipolar electrode configuration before it was recorded with a multifunction data acquisition device (USB-6361, National Instruments) with an A/D converter resolution of 16 bits between the analog input range of ± 10 V and with a maximum sampling rate of 1 MS/s. The sampling rate was set to 40 kHz for the measurements performed in this article. Care has been taken that the noise contribution of the A/D converter is negligible by the sufficient preamplification of the sensor signals. This device is also used to generate biphasic impulses, as generally applied for clinical neurostimulators, by adjusting the stimulation frequency f_s, pulsewidth of the stimulation t_p, and the amplitude A in voltage, as shown in Fig. 4(a). A dc component in the signal is avoided by a negative pulse with the same pulsewidth–voltage product.

D. Biot–Savart Law

This section briefly gives two different equations to calculate the total magnetic field B with the Biot–Savart law for two approaches, which are of interest in this article. The magnetic field for a straight wire can be calculated using the Biot–Savart law for a current-carrying finite straight wire [28] with the following equation:

$$B(i) = \frac{\mu_0 I}{4\pi\, D(i)}(\cos(\alpha) - \cos(\beta)) \tag{1}$$

where the wire carries the current I at a distance $D(i)$ to the ith sensor with the identified end points by the angles α and β, $\mu_0/(4\pi)$ is a constant, and $B(i)$ is the magnetic flux density at $D(i)$. We will see that this formula can be used as a good approximation for the monopolar electrode configuration.

The magnetic field for a current dipole can be calculated with the Biot–Savart law for a single current dipole [14]

$$B(i) = \frac{\mu_0}{4\pi} \frac{(\vec{R}(i) - \vec{L}) \times \hat{s}(i) \cdot \vec{Q}}{|\vec{R}(i) - \vec{L}|^3} \tag{2}$$

where $\vec{Q}$ is the dipole moment, $\vec{L}$ is the dipole location (represented as a green dot marker in Fig. 3), $\vec{R}(i)$ is the ith sensor location [represented as a red dot marker in Fig. 1(a)], and $\hat{s}(i)$ is the unit orientation of the ith sensor. It will be shown that this equation fits the bipolar electrode configuration and will be used for electrode localization. At this point, it is

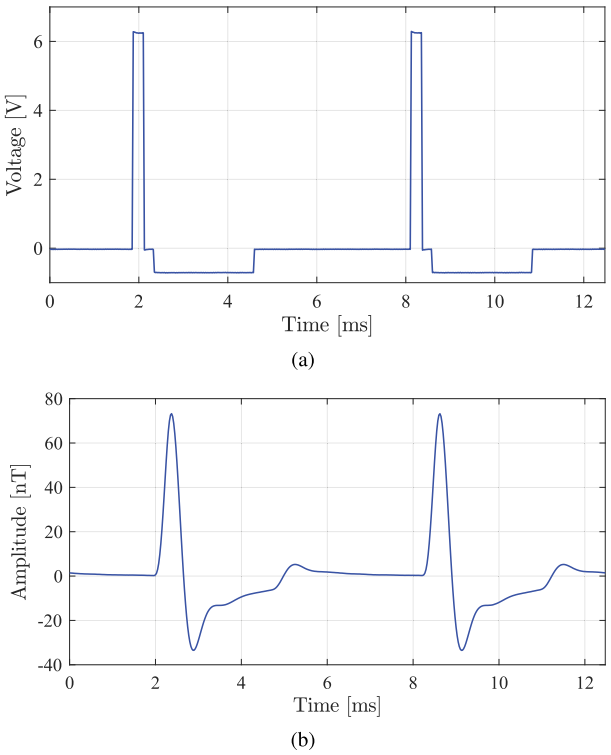

Fig. 4. (a) Created stimulation signal with an amplitude of $A = 6.3$ V, a pulsewidth of $t_p = 240$ μ s, and a frequency of $f_s = 160$ Hz. (b) The measured signal with the fluxgate sensor with 80 averaging for monopolar electrode configuration.

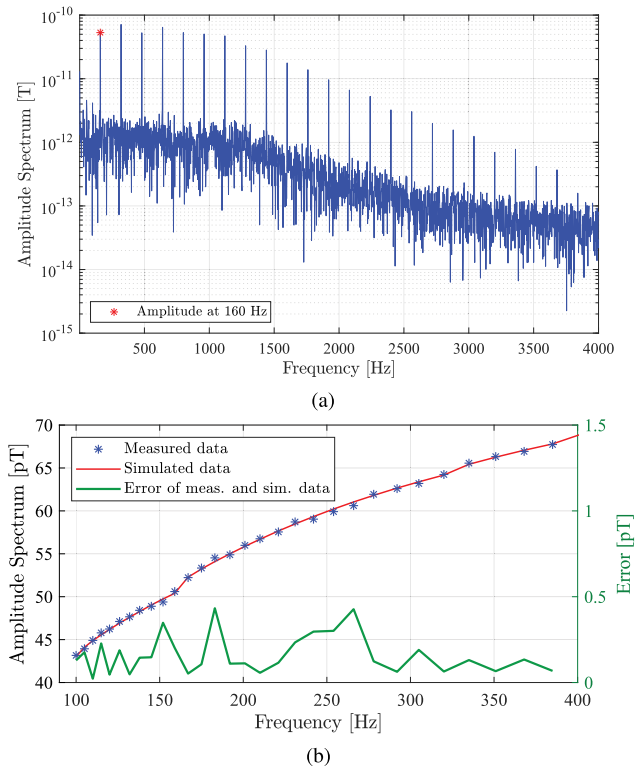

Fig. 5. (a) Amplitude spectrum in T of the stimulation signal with an amplitude of $A = 6.3$ V for bipolar mode is shown. Red asterisk marker: amplitude value at the 160-Hz fundamental frequency. (b) Measured and simulated amplitude values and the error between both values in pT at the fundamental frequency, if it is varied between 100 and 385 Hz for bipolar electrode configuration with a constant stimulation amplitude of 6.3 V.

assumed that the dipole points in the direction of the negative z-axis, considering that the electrode in the phantom head is arranged parallel to the z-axis, and thus, the current flows in this direction ($\hat{s} = [0, 0, -1]$). Since we are only interested in the position of the electrode and the dipole orientation is not considered for the localization algorithm described in Section III-D, it will not be discussed further.

III. Results

For all the following results, a relatively strong stimulation signal with an amplitude of $A = 6.3$ V, a pulsewidth of $t_p = 240$ μs, and a frequency of $f_s = 160$ Hz, as shown in Fig. 4(a), was used. The motivation of this choice is included in Section IV.

A. Signal Analysis

In order to examine the shape of the measured deep-brain stimulation signal with the fluxgate sensor, the electrode was monopolarly stimulated and the tangential magnetic component was measured 1 s at a distance of about 45 mm. The measured signal (80 times averaged) is shown in Fig. 4(b). The measured signal is already visible in the time domain, since the magnetic flux density generated by the monopolar stimulation is relatively strong and has a peak amplitude of about 73 nT. The shape of the recorded signal is due to sensor properties that has a bandwidth of 1 kHz and, thus, acts as a low-pass filter.

Furthermore, the electrode was bipolarly stimulated with a constant pulsewidth of $t_p = 240$ μs and a frequency of $f_s = 160$ Hz. The amplitude spectrum is shown in Fig. 5(a) for a constant stimulus voltage. Increasing the stimulation voltage between 0.5 and 7 V showed a linear increase in the resulting magnetic flux density between approximately 5 and 50 pT, as can be expected for a homogeneous model with only one conductivity. Nevertheless, an increase in the stimulation frequency at a constant stimulation voltage leads to a nonlinear increase in the magnetic field, which was measured and can be seen in Fig. 5(b). For this purpose, a constant stimulation amplitude of 6.3 V was selected, the stimulation frequency was changed logarithmically between 100 and 385 Hz, each 60-s recording was transformed into the frequency domain using Welch's method [29] with the Hanning window, and finally, the amplitude value from the amplitude spectrum at the correspondingly adjusted fundamental frequency was taken. The increase in the magnetic field over the investigated frequency can be interpreted as an increase in the electrical conductivity between the used contacts for the bipolar electrode configuration over the frequency. The magnitude of the impedance between both the contacts was measured and decreases nonlinearly from about 380 Ω for 100 Hz to 240 Ω for 385 Hz, and thus, the current gets higher with the same behavior. This finally leads to an increase with the same slope in the magnetic field. The error between the measured data with the fluxgate sensor and the simulated data based on the

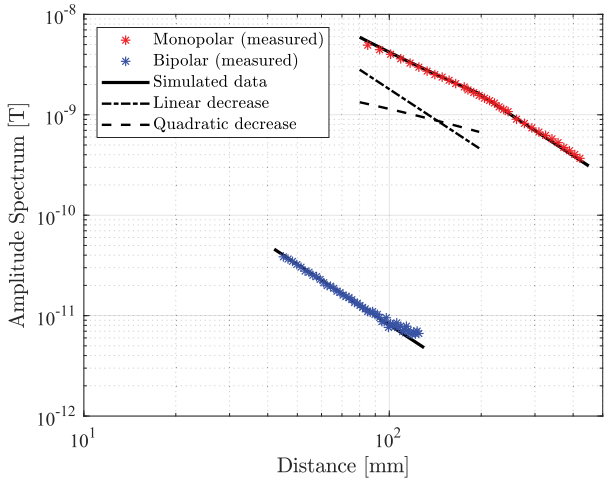

Fig. 6. Decrease in the amplitude spectrum at the fundamental frequency in T dependent on the distance in mm for both monopolar (blue curve) and bipolar (red curve) electrode configurations. At a distance of 45 mm, there is about 40 pT of magnetic field in bipolar mode (red asterisk marker).

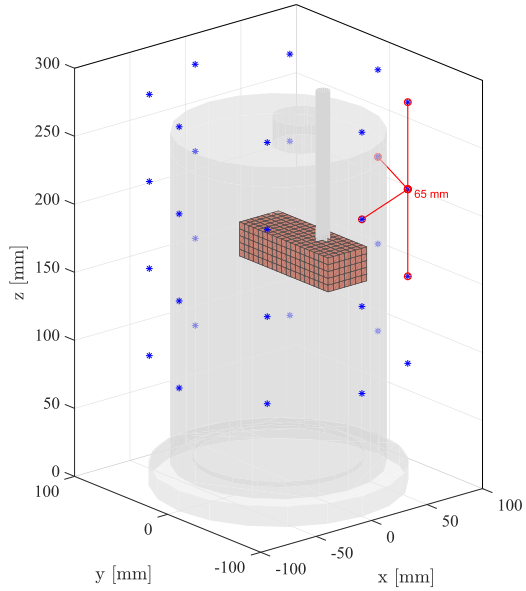

Fig. 7. Cylindrical head model surrounded by 32 measuring points in blue asterisks in a symmetrical measuring system and eight points each at one measuring height. As an example, a part of the whole volume is shown, which has been divided into small voxels with an edge length of 5 mm.

measured magnitude impedance is less than 0.4 pT for all performed measurements [see Fig. 5(b)], i.e., a maximum of about 1 % inaccuracy of the measured magnetic field values.

B. Distance Dependence

To investigate which field strengths are to be expected in both the monopolar and bipolar electrode configurations at which distance, the following measurement was performed. The stimulation parameters as described at the beginning of this chapter were used. The tangential magnetic component was measured with the fluxgate sensor 1 s for the monopolar and 10 s for the bipolar mode at the height of the electrode. The measurement distance varied between 85 and 421 mm with a step size of 3 mm for the monopolar and between 45 and 125 mm with a step size of 1 mm for the bipolar mode. Again, each measured time signal is transformed into the frequency domain using Welch's method, and the amplitude value from the amplitude spectrum at 160 Hz is then taken.

The results are shown in Fig. 6 in a double logarithmic scale. The magnetic field in the monopolar mode (e.g., about 5 nT at a distance of 85 mm) compared with bipolar stimulation (about 10 pT at the same distance) is about more than 100 times stronger. At larger distances, the resulting magnetic field of the bipolar stimulation is strongly affected by the sensor noise, causing fluctuation in the bipolar measured values (blue asterisk markers). Furthermore, the magnetic field of both the electrode configurations decreases differently over the distance. It decreases quadratically in the bipolar stimulation mode; and first linearly and then quadratically in the monopolar mode, which can be explained by the current flow in the system and confirms the following assumptions: The current flow between the two middle contacts of the electrode (bipolar), which corresponds to approximately 3 mm, is assumed to be a current dipole at the considered distances between 45 and 125 mm, so that the resultant magnetic field decreases quadratically according to (2), in which relation $B \propto 1/R^2$ applies. The (calculated) simulated values were inserted as a black line in the figure, which shows the agreement of the measured and simulated data. In the case of monopolar stimulation, where the current flows over the entire height of the phantom head, the resultant field decreases linearly, according to (1), in which field B is directly proportional to $1/D$. In addition, with the increasing distance, when it reaches the same order of the phantom dimension, the current flow behaves like a dipole, and the field then starts to decrease quadratically, as some lines previously described.

C. Monopolar and Bipolar Analyses

For the analysis of the magnetic field distribution for both monopolar and bipolar electrode configurations, the following measurement was performed: The stimulation signal, as shown in Fig. 4(a), has been used for both the modes. Since each measurement with different electrode positions marked with black dots in Fig. 2 showed qualitatively the same behavior, the measurement with the electrode position at $a = 40$ mm will be presented here.

In the case of monopolar stimulation, the lowest contact of the electrode is chosen to be the cathode (contact 0 in Fig. 3), and in the case of bipolar stimulation, the middle two contacts are used as the cathode and the anode (contacts 1 and 2 in Fig. 3). The measurement took place at 32 measuring points with a radius of approximately 85 mm, divided over four heights with a distance of 65 mm, as shown in Fig. 7 with blue asterisk markers. The neighboring measuring points are also 65 mm apart to guarantee a symmetrical measuring system. The measuring points were located at the distance between 45 mm (closest distance) and 125 mm (farthest distance) to the electrode, as shown in Fig. 2. In the monopolar case, the magnetic field is measured for 1 s at each of these measuring points in all three orthogonal directions, whereas in the bipolar case, it was measured for 10 s.

Thus, the total measurement time varies between 10 min (monopolar) and 30 min (bipolar), including the movement of the head scanner, the rotation of the sensor, the storage process of the measured data, and the 1-s break before each recording to remove vibration artifacts in the system.

Each measured time signal is transformed into the frequency domain using Welch's method, the amplitude value from the amplitude spectrum at the 160-Hz fundamental frequency is taken, and the magnitude of the magnetic flux density at each point is calculated, which results in a total of 32 values representing the measured magnetic field distribution. For a better graphical visualization, interpolation between these values is then performed. The result for the field distribution of the monopolar and bipolar electrode configurations can be seen in Fig. 8. The field distribution in the top figure is generated by the current, which flows from the signal generator through the conductors over the entire height of the cylinder and under the cylinder back to the generator. Thus, a relatively large magnetic flux density in the nT range is generated over the entire measuring surface. The contribution of the field generated by the current in the conductor placed parallel to the cylinder is most evident in contrast to the field generated by the current flowing through the cylinder, which is visible as the red area in the figure. The measured magnetic field distribution of the monopolar stimulation for the same electrode location can thus be calculated theoretically as an approach using the Biot–Savart law for a current-carrying finite straight wire with [see (1)]. The calculated result is shown in Fig. 9(a), which only considers the field generated by the current in the cylinder and neglects the influence of the signal cable.

The measured field distribution in the bipolar case [see Fig. 8(b)] is, in contrast to that of the monopolar one, caused only by the current flowing between the two contacts of the electrode, resulting in about 100 times weaker magnetic flux density in the pT range. In the blue area, the distance of the measuring points to the electrode is already so large that the magnetic field strength disappears in the noise level of the sensor. The magnetic field caused by the current in the conductor is completely removed, since the current flowing through the conductor to the electrode flows back through the conductor parallel and in close vicinity to the feeding conductor, so that their contributions cancel out each other. Hence, the stimulation mode can be modeled as an electrical current dipole. For the calculation of its field distribution, the Biot–Savart law for a single current dipole according to (2) can be used. The theoretically calculated magnetic field distribution for the same electrode location can be seen in Fig. 9(b) showing qualitatively the same behavior. The normalized root-mean-square error (NRMSE) between the measured magnetic field distributions of the bipolar electrode configuration [Fig. 8(b)] and the simulated magnetic field distribution [Fig. 9(b)] can be seen in Fig. 9(c). The error varies between about 0% and 12%, depending on how far the measuring points are placed to the electrode. At short distances, the error is comparatively small (between about 0% and 2%), since the magnetic field generated by the stimulation can be measured by the fluxgate sensor. At larger distances, the error increases significantly up to 12%, because

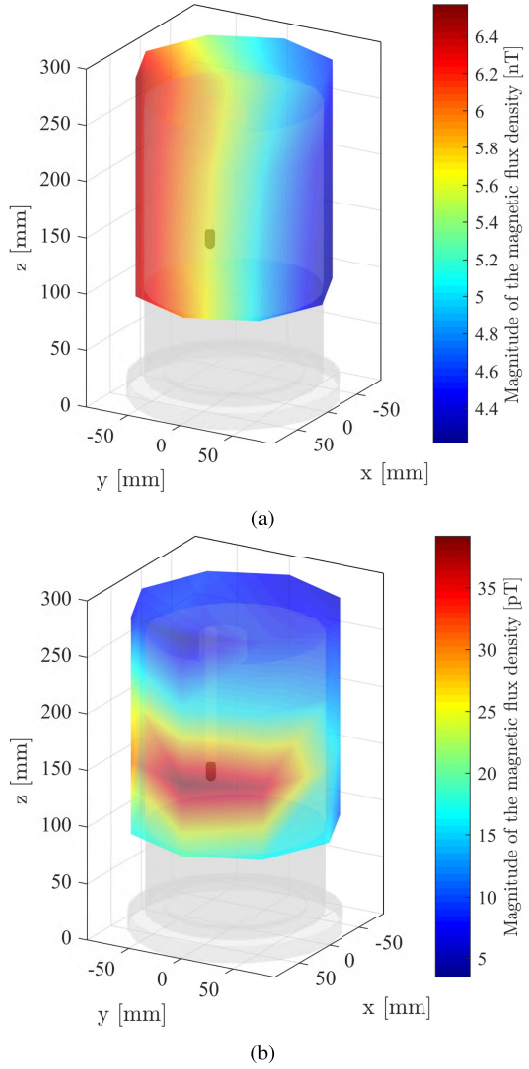

Fig. 8. Measured magnetic field distribution of (a) monopolar and (b) bipolar electrode configuration created by 32 measuring points. The magnitude of the magnetic flux density at each measuring point was calculated and interpolated between the points.

the measuring range is limited by the noise level of the fluxgate sensor and the generated magnetic field disappears in the sensor noise.

In order to localize the DBS electrode in the cylindrical head model by such magnetic field measurements, it is required to have a concentrated spatial field distribution, as in the case of bipolar stimulation. However, it has to be dealt with very weak magnetic fields in the pT range. In the case of monopolar stimulation, the magnetic field is much stronger, but no information about the electrode height can be obtained. Furthermore, the superimposition of the magnetic field through the conductor has also to be considered, which anyway limits the localization accuracy of the electrode.

D. Localization of the Electrode

The bipolar analysis has shown that the model of an electrical current dipole fits the bipolar electrode configuration. The assumption is confirmed by an exemplary successful DBS

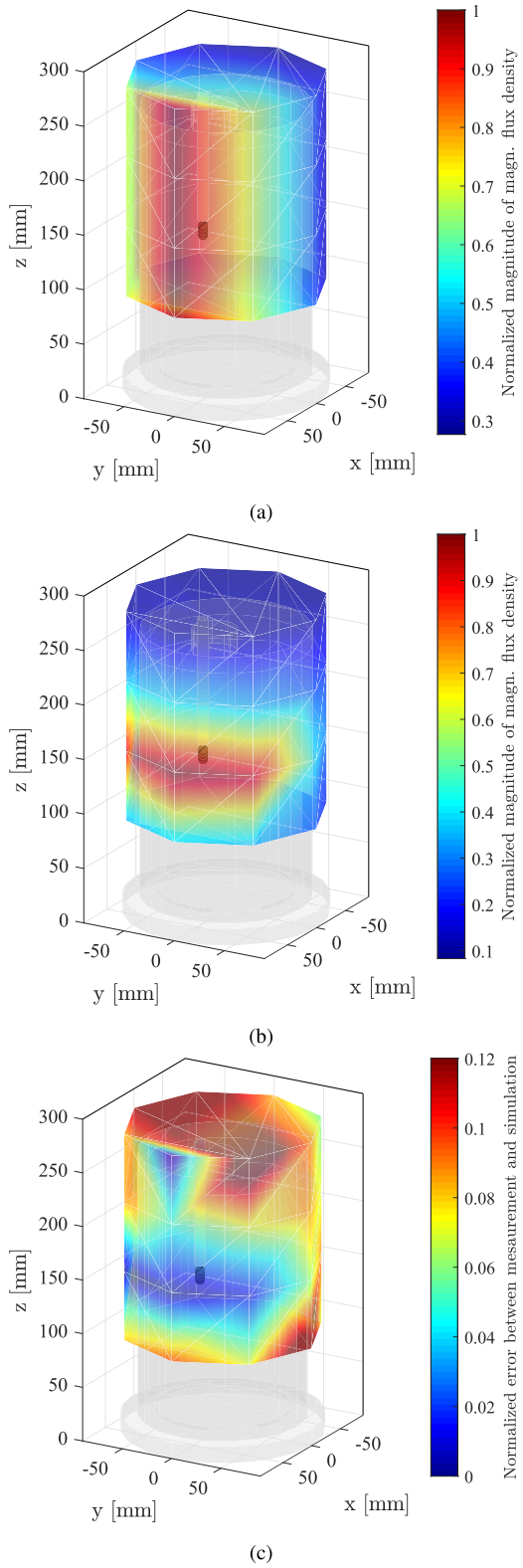

Fig. 9. Theoretically calculated field distribution of (a) monopolar and (b) bipolar electrode configurations with (1) and (2) for the same electrode location as in Fig. 8. The normalized magnitude of the magnetic flux density at each simulated point was calculated. (c) NRMSE of the measured [see Fig. 8(b)] and simulated [see Fig. 9(b)] data are shown.

electrode localization, which will be presented in this section. Since the exactly placed electrode does not move and does not rotate, and there is only one active source in the model, a dipole fitting algorithm can be used, which searches for a source that best describes the measured data. The volume to be examined is divided into small voxels and the forward-computed magnetic flux density with (2) is compared with those calculated from the measured data. The programed and used dipole-fit algorithm is mainly divided into five algorithm steps.

1) Calculate the magnitude of the magnetic flux density in tesla at each ith measurement of the sensor. Therefore, each measured time signal has to be transformed into the frequency domain and the amplitude in the spectrum at the adjusted stimulation frequency has to be taken. The result will be the measured magnitude of the magnetic flux density $|B_{\mathrm{meas}}|(i)$. It is a vector with the length of $\mathrm{N_{meas}}$ (total number of measuring points i).
2) Consider only the elements of $|B_{\mathrm{meas}}|$ at the measuring points j, where the magnetic flux density could be calculated and did not get lost in the noise. The well-known noise level of the used measuring sensor can be selected as a threshold value. Then, normalize the remaining values to their maximum value to get $|B_{\mathrm{meas,norm}}|(j)$. The maximum value is the strongest measured magnetic field, which comes from the measurement at the closest measuring point to the electrode. It is a vector with the length of $\mathrm{N_s}$ (total number of considered measuring points j, $\mathrm{N_s} \leq \mathrm{N_{meas}}$).
3) Divide the region to be examined into small 1 mm $\times$ 1 mm voxels, where each voxel gets a voxel number and its Cartesian coordinates. Then, calculate the expected magnitude of the magnetic flux density in Tesla over the same chosen sensor positions j with (2) and normalize it to its maximum element in the vector. The result will be the modeled magnetic flux density $|B_{\mathrm{model,norm}}|(j,n)$. It is a matrix with the dimension $\mathrm{N_s} \times \mathrm{N_v}$, where $\mathrm{N_v}$ represents the total number of considered voxels n.
4) Define the dipole-fit cost function and determine the specific error for all voxel n

$$e(n) = \sum_{j=1}^{\mathrm{N_s}} (|B_{\mathrm{meas,norm}}|(j) - |B_{\mathrm{model,norm}}|(j,n))^2 \qquad (3)$$

where $\mathrm{N_s}$ represents the total number of chosen measuring points in Step 2 of the algorithm. $e(n)$ is a vector with the length of $\mathrm{N_v}$.
5) Take the global minimum value of the dipole-fit cost function

$$\min[e(n)] = e(n_{\mathrm{dipole}}). \qquad (4)$$

The voxel n_{dipol} represents the smallest error and is the result of the localization algorithm. The calculated magnetic flux density for this voxel best explains the measured data with the error $e(n_{\mathrm{dipol}})$.

For the exemplary fluxgate measurement to be shown here, the electrode was placed at $a = 40$ mm, it was bipolarly stimulated with the stimulation parameters as described previously, and the lower two contacts are used with the physical center at the Cartesian coordinates $[x_d, y_d, z_d] = [40,\ 0,\ 179\ \mathrm{mm}]$. The measuring time at each measuring points was set to 10 s,

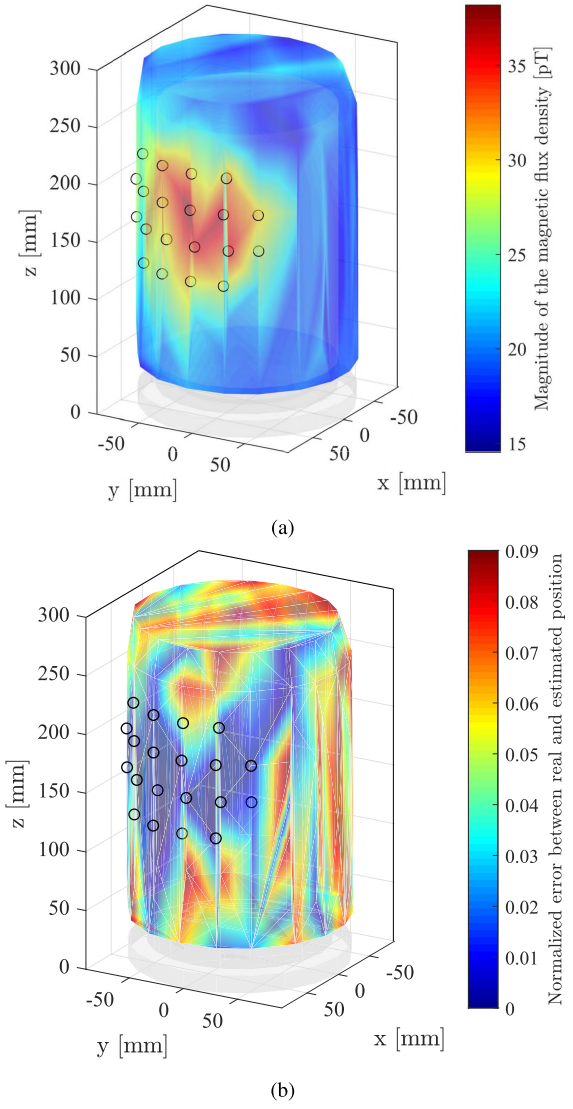

Fig. 10. (a) Measured field distribution of bipolar electrode configuration created by 176 sensor points. The magnitude of the magnetic flux density at each measuring point was calculated and interpolated between the points. The sensor points where the magnetic fields are visible were marked in black circles. (b) NRMSE between the real position of the electrode and the position estimated by the localization algorithm.

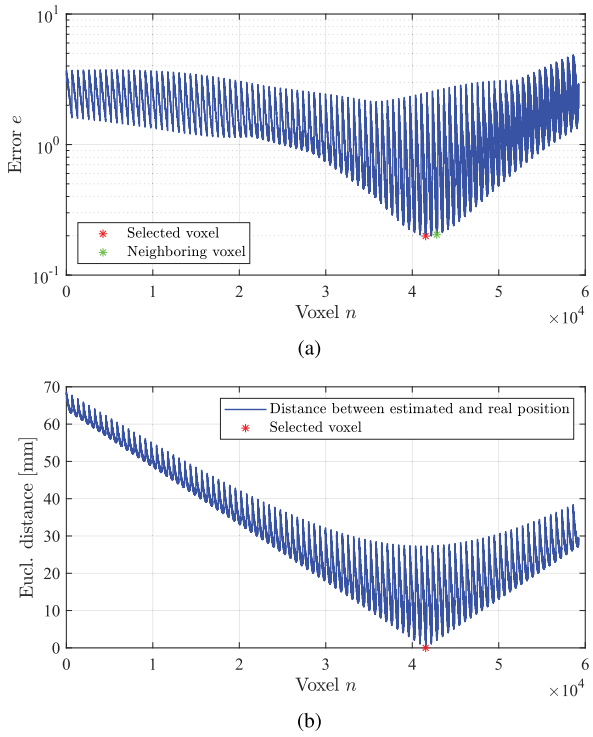

Fig. 11. (a) Calculated error e over all voxel n. The voxel that illustrates the smallest error at the global minimum is selected (red asterisk). The second smallest error is caused by the neighboring voxel (green asterisk). (b) Euclidean distances in millimeter over the same voxel n. The selected voxel has a distance of 0 mm to the real position of the electrode.

and a total of 176 measuring points, 22 points at eight heights, was selected. The sensor points were located at the distance between 45 and 125 mm to the fixed electrode. The measured field distribution is shown in Fig. 10(a). In Step 2 of the algorithm, only 20 of 176 measuring points were considered due to the field shown in blue that was basically the noise level of the fluxgate sensor. The considered measuring points are represented with black circles in Fig. 10. The threshold value chosen here at 30 pT was slightly higher than the sensor noise level to remove measurement inaccuracies and variations just above the noise level. The region was divided into 1 mm^3 voxels in which the electrode was searched in the x-direction from 19 to 50 mm, in the y-direction from -31 to 60 mm, and in the z-direction from 173 to 194 mm in a total number of about $N_s = 60\,000$ voxels. For each of these voxels, its voxel number and its Cartesian coordinates are known. The Euclidean distances between these voxels and the real position of the electrode are shown in Fig. 11(b). The region to be examined can be seen in Fig. 7, which was subdivided with a voxel edge length of 5 mm. For each voxel, the corresponding error $e(n)$ is calculated with (3) and is shown in Fig. 11(a). The voxel number $n_{\text{dipole}} = 41\,548$ illustrates the smallest error at the global minimum of about $e(n_{\text{dipole}}) = 0.2$ and represents the solution found at the same Cartesian coordinates of the electrode $[x_d, y_d, z_d] = [40\text{ mm},\ 0\text{ mm},\ 179\text{ mm}]$. Therefore, the distance between the position of the physical center of the used bipolar electrode configuration and the voxel that yielded the smallest error in the calculation is 0 mm [see Fig. 11(b)]. The NRMSE between the real position of the electrode and the position estimated by the localization algorithm can be seen in Fig. 10(b). At the considered measuring points (black circles), the errors are between 0% and 1%, which led to an accurate localization. At the other measuring points, errors of up to 10% can be seen, which were neglected in Step 2 of the algorithm, as they would lead to a shifting of the found position. The direct neighbor voxel ($n_{\text{neighbor}} = 42\,199$) with the Cartesian coordinates $[x_n, y_n, z_n] = [41\text{ mm},\ 0\text{ mm},\ 179\text{ mm}]$ has a distance of 1 mm to the real position and reaches the second smallest error [see Fig. 11(a)]. Since the distribution of the volume into voxels is done by first arranging the voxels in the z-direction, then arranging them in the y-direction, and then in the x-direction, jumps occur after the last arranged voxel at the end of each direction to get higher with the distribution plane.

Thus, the distance of the voxel to the electrode changes rapidly and such value jumps of the errors occur, as shown in Fig. 11. Therefore, the number of the neighboring voxels $n_{\text{neighbor}} = 42\,199$ is not directly adjacent to the found voxel $n_{\text{dipole}} = 41\,548$.

The entire measurement took about 2 h of time and the computing time was significantly reduced by the second step of the algorithm. It has been shown that the model of an electrical current dipole can be assumed for the bipolar electrode configuration and that localization can be performed with this model assumption at least at an electrode position near to the surface. For a more accurate validation of the localization feasibility, further measurements have to be made, which will be part of our further work.

IV. Discussion

The magnetic field properties for both the monopolar and bipolar electrode configurations of a deep-brain stimulation electrode were analyzed in this article with 3-D magnetic field measurements using the fluxgate sensor as a unidirectional magnetometer. Therefore, the electrode was placed in a cylindrical simplified phantom head that has been developed to match the dimensions of a human head. Such a geometrically well-defined model is needed as a first step in measuring the precise position of the deep-brain stimulation electrode. In further steps, it will also be important for electrode reconstruction algorithms for validating the localization accuracy. That was the motivation for this article.

Since the fluxgate sensor has a frequency bandwidth of 1 kHz, it acts as a low-pass filter during recording, and the recorded signal, thus, mainly includes the applied stimulation frequency of 160 Hz and its next five harmonics (320, 480, 640, 800, and 960 in hertz). Nevertheless, the shape of the stimulation signal was still clearly visible. The whole analysis in this article took place in the frequency domain by taking the amplitude value from the amplitude spectrum at the fundamental frequency. It is also possible to take any other harmonic frequency below 1 kHz by using the fluxgate sensor. Other magnetic sensors with a smaller bandwidth detecting one of these frequencies of interest would also be sufficient, e.g., thin-film magnetoelectric sensors (ME sensors) [30], which are being developed within the framework of the Collaborative Research Center CRC 1261.

The field strengths of the monopolar electrode configuration were in the nT-range and decrease linearly over the considered distance. Since the magnetic field at the measuring points is superimposed by the fields generated by the current flowing through the whole system, the field generated only by the current in the cylinder cannot be determined due to the influence of the signal cable. Therefore, the monopolar stimulation modeled approximation as a current-carrying conductor cannot be used for electrode localization. In addition, there is no information about the height of the electrode (z-coordinate) that already limits the localization possibility. In contrast, the bipolar electrode configuration allows a more focused spatial resolution in the field distribution, which could be estimated by the model of an electrical current dipole and could be used for electrode localization. However, the field strength is 100 times weaker than the field generated by monopolar stimulation, and it decreases quadratically with the distance to the sensor. Therefore, it is feasible to estimate the magnetic field strengths at any desired location within the described limits to enable the electrode localization with magnetic sensor measurements.

While we acknowledge that further work is necessary to achieve a more accurate validation of localization methods, the localization result in this article shows that the basic dipole fitting algorithm was able to detect the position of the electrode in the simplified cylindrical phantom head. In a more realistic scenario, the following difficulties need to be addressed, and the localization algorithm has to be adapted to that. The real human head with different brain structures is more complicated. This model has to be extracted from high-resolution MR or CT images of the patient. Since the implanted areas of interest are known and the current of the DBS is only flowing in a particular known region, the segmentation of this images can be specified on this region resulting in a higher quality. The localization method must use the resultant segmented head model to divide the entire head into small voxels. Each voxel has its own electrical conductivity, which also differs from our homogeneous model with only one conductive material. The used voltage-controlled stimulation regulates the voltage by changing the current depending on the resistance, which is different in each individual anatomy of the patients. Changes in the current lead to a change of the strength of the magnetic field. Thus, the magnetic field, which is calculated in Step 3 of the algorithm, becomes even more difficult. This problem can be solved by using a newer current-controlled DBS system (e.g., Vercise Cartesia electrode, Boston Scientific Corporation), in which the current can be adjusted to any individual anatomy, which in turn leads to a constant magnetic field. Different conductivities would therefore no longer be a problem for the described algorithm, which is still under investigation in our research. In addition, the angle at the implantation of the DBS electrode is also unknown, which was assumed to be vertical in our model. This will lead to a variable orientation of the magnetic field. Since the algorithm, as described here, works with the magnitude of the magnetic field and not with its orientation, the problem can be neglected. Furthermore, the magnetic field measurements with real DBS patients using only one magnetic sensor, measuring around the head point for point, will also be a challenge due to the long measuring time on the one hand and the head movement of the patient during the measurement on the other hand. An array of sensors will reduce the time significantly, and the movement of the head can be detected and corrected, e.g., with nonmagnetic cameras inside the shielded chamber recording the shifting of the head to correct the position of the sensor in relation to the head surface.

The parameters of the used stimulation signal over all performed measurements were set at relatively high values with 6.3-V amplitude and 240-μs pulsewidth, to take advantage of the phantom head ending up with larger magnetic fields. The same choice of the stimulation amplitude cannot be applied in a real head of a DBS patient, as this would not be tolerated

by the patient. Since the magnetic field generated by the stimulation is linearly dependent on the stimulation amplitude for the investigated frequency, it can be assumed that the field strengths caused by the amplitude commonly set between 1 and 4 V in a real head are smaller by a factor of between $6.3/1 = 6.3$ and $6.3/4 = 1.6$ than the measured values. This can be interpreted as an estimated calculation in order to get an idea of an approximate magnitude of the generated magnetic fields in real DBS patients, considering that the electrical conductivity of the physiologic saline solution used in the cylindrical head model is comparable with that of a human brain and that the investigated frequency is adjusted in the patient.

V. Conclusion

This article demonstrates that the magnetic field of the deep-brain stimulation electrode can be measured with magnetic fluxgate sensors at a distance between 45 and 125 mm, and there are differences in the magnetic properties of both the monopolar and bipolar electrode configurations. The magnetic flux densities are in the pT range in the bipolar stimulation mode and decrease quadratically with distance. In the monopolar mode, the fields are in the nT range and decrease first linearly and then quadratically with distance. Furthermore, it has been shown that measuring with the bipolar mode gives us a more focused spatial magnetic field distribution, which is essential for electrode localization, where the stimulation mode can be modeled as an electrical current dipole. As a proof of feasibility, we presented a bipolar measurement in which the model assumed in the dipole-fit algorithm accurately localized the electrode. We acknowledge that further work is necessary to achieve a more accurate validation of localization methods and results. Although the monopolar stimulation generates a 100 times larger magnetic field, it is less suited to be used for electrode localization due to the corresponding field distribution, which is the superposition of magnetic fields from the cables, and does not provide any information about the height of the electrode in the head phantom.

References

[1] G. Deuschl *et al.*, "A randomized trial of deep-brain stimulation for Parkinson's disease," *New England J. Med.*, vol. 355, no. 9, pp. 896–908, 2006.

[2] A. Kupsch *et al.*, "Pallidal deep-brain stimulation in primary generalized or segmental dystonia," *New England J. Med.*, vol. 355, no. 19, pp. 1978–1990, 2006.

[3] J. M. Nazzaro, K. E. Lyons, and R. Pahwa, "Deep brain stimulation for essential tremor," in *Handbook of Clinical Neurology*, vol. 116, A. M. Lozano and M. Hallett, Eds. Amsterdam, The Netherlands: Elsevier, 2013, pp. 155–166.

[4] S. Hemm and K. Wårdell, "Stereotactic implantation of deep brain stimulation electrodes: A review of technical systems, methods and emerging tools," *Med. Biol. Eng. Comput.*, vol. 48, no. 7, pp. 611–624, 2010.

[5] C. R. Butson and C. C. Mcintyre, "The use of stimulation field models for deep brain stimulation programming," *Brain Stimulation*, vol. 8, no. 5, pp. 976–978, 2015.

[6] C. R. Butson and C. C. McIntyre, "Current steering to control the volume of tissue activated during deep brain stimulation," *Brain Stimulation*, vol. 1, no. 1, pp. 7–15, Jan. 2008.

[7] C. Schmidt and U. van Rienen, "Modeling the field distribution in deep brain stimulation: The influence of anisotropy of brain tissue," *IEEE Trans. Bio-Med. Eng.*, vol. 59, no. 6, pp. 1583–1592, Jun. 2012.

[8] C. Schmidt and U. van Rienen, "Adaptive estimation of the neural activation extent in computational volume conductor models of deep brain stimulation," *IEEE Trans. Biomed. Eng.*, vol. 65, no. 8, pp. 1828–1839, Aug. 2018.

[9] A. Motevakel and A. Medvedev, "Localization of deep brain stimulation electrodes via metal artifacts in CT images," in *Proc. 36th Annu. Int. Conf. IEEE Eng. Med. Biol. Soc. (EMBC)*, Aug. 2014, pp. 1055–1058.

[10] S. H. Paek, J. H. Han, J.-Y. Lee, C. Kim, B. S. Jeon, and D. G. Kim, "Electrode position determined by fused images of preoperative and postoperative magnetic resonance imaging and surgical outcome after subthalamic nucleus deep brain stimulation," *Neurosurgery*, vol. 63, no. 5, pp. 925–936, 2008.

[11] C. Pollo *et al.*, "Localization of electrodes in the subthalamic nucleus on magnetic resonance imaging," *J. Neurosurg.*, vol. 106, no. 1, pp. 36–44, 2007. doi: 10.3171/jns.2007.106.1.36.

[12] C. W. O. Lopez, O. Escobar, G. A. Uribe, X. Garcia, L. Furlanetti, and J. A. E. Martinez, "A series of 80 consecutive cases of dystonia: A neurosurgical treatment algorithm," *J. Neural Transmiss.*, vol. 120, no. 7, pp. 1141–1142, 2013.

[13] J. Y. Lee *et al.*, "Is MRI a reliable tool to locate the electrode after deep brain stimulation surgery? Comparison study of CT and MRI for the localization of electrodes after DBS," *Acta Neurochirurgica*, vol. 152, no. 12, pp. 2029–2036, 2010.

[14] J. C. Mosher, P. S. Lewis, and R. M. Leahy, "Multiple dipole modeling and localization from spatio-temporal MEG data," *IEEE Trans. Biomed. Eng.*, vol. 39, no. 6, pp. 541–557, Jun. 1992.

[15] P. Hansen, *MEG: An Introduction to Methods*. New York, NY, USA: Oxford Univ. Press, 2010.

[16] J. W. Wheless *et al.*, "Magnetoencephalography (MEG) and magnetic source imaging (MSI)," *Neurologist*, vol. 10, no. 3, pp. 138–153, 2004.

[17] P. Hayes *et al.*, "Electrically modulated magnetoelectric sensors," *Appl. Phys. Lett.*, vol. 108, no. 18, Apr. 2016, Art. no. 182902.

[18] X. Jun, L. Luming, and H. Hongwei, "Primary experimental study on safety of deep brain stimulation in RF electromagnetic field," in *Proc. Annu. Int. Conf. IEEE Eng. Med. Biol. Soc.*, Sep. 2009, pp. 3091–3094.

[19] E. M. Wassermann and T. Zimmermann, "Transcranial magnetic brain stimulation: Therapeutic promises and scientific gaps," *Pharmacol. Therapeutics*, vol. 133, no. 1, pp. 98–107, 2012.

[20] M. A. Nitsche *et al.*, "Transcranial direct current stimulation: State of the art 2008," *Brain Stimulation*, vol. 1, no. 3, pp. 206–223, 2008.

[21] J. Fan, J. L. X. Li, J. Li, T. C. Wu, and X. Li, "Magnetic field projector for deep brain stimulation," *IEEE Trans. Magn.*, vol. 51, no. 11, Nov. 2015, Art. no. 5400204.

[22] C. Pollo, J.-G. Villemure, F. Vingerhoets, J. Ghika, P. Maeder, and R. Meuli, "Magnetic resonance artifact induced by the electrode activa 3389: An *in vitro* and *in vivo* study," *Acta Neurochirurgica*, vol. 146, no. 2, pp. 161–164, Feb. 2004.

[23] B. Brahimaj, R. B. Kochanski, and S. Sani, "Microelectrode accuracy in deep brain stimulation surgery," *J. Clin. Neurosci.*, vol. 50, pp. 58–61, Apr. 2018.

[24] M. I. Iacono, S. R. Atefi, L. Mainardi, H. C. Walker, L. M. Angelone, and G. Bonmassar, "A study on the feasibility of the deep brain stimulation (DBS) electrode localization based on scalp electric potential recordings," *Frontiers Physiol.*, vol. 9, p. 1788, Jan. 2019.

[25] J. Volkmann, J. Herzog, F. Kopper, and G. Deuschl, "Introduction to the programming of deep brain stimulators," *Movement Disorders*, vol. 17, no. S3, pp. S181–S187, 2002.

[26] J. Volkmann, E. Moro, and R. Pahwa, "Basic algorithms for the programming of deep brain stimulation in Parkinson's disease," *Movement Disorders*, vol. 21, no. S14, pp. S284–S289, 2006.

[27] J. Buhlmann, L. Hofmann, P. A. Tass, and C. Hauptmann, "Modeling of a segmented electrode for desynchronizing deep brain stimulation," *Frontiers Neuroengineering*, vol. 4, p. 15, Dec. 2011. [Online]. Available: http://journal.frontiersin.org/article/10.3389/fneng.2011.00015/abstract

[28] J. A. Miranda, "Magnetic field calculation for arbitrarily shaped planar wires," *Amer. J. Phys.*, vol. 68, no. 3, pp. 254–258, Mar. 2000. [Online]. Available: http://aapt.scitation.org/doi/10.1119/1.19418

[29] P. D. Welch, "The use of fast Fourier transform for the estimation of power spectra: A method based on time averaging over short, modified periodograms," *IEEE Trans. Audio Electroacoust.*, vol. AU-15, no. 2, pp. 70–73, Jun. 1967.

[30] R. Jahns, R. Knöchel, H. Greve, E. Woltermann, E. Lage, and E. Quandt, "Magnetoelectric sensors for biomagnetic measurements," in *Proc. IEEE Int. Symp. Med. Meas. Appl.*, May 2011, pp. 107–110.

Mevlüt Yalaz received the M.Sc. degree in electrical and information engineering from the University of Kiel, Kiel, Germany, in 2016, where he is currently pursuing the Ph.D. degree with the Chair for Microwave Engineering and the Department for Neurology.

His current research interests include magnetic field measurements, digital signal processing, source localization for deep brain stimulation, and modeling of its stimulated fields.

Alexander Teplyuk received the diploma degree in technology of aircraft construction from National Aerospace University, Kharkov, Ukraine, in 2000, and the Dr.Ing. degree from Kiel University, Kiel, Germany, in 2012.

From 2001 to 2006, he was a Research Engineer with the Radar Department, Institute of Radiophysics and Electronics, National Academy of Sciences of Ukraine, Kiev, Ukraine. Since 2012, he has been a Research Fellow with the Microwave Department, Faculty of Engineering, Kiel University. His current research interests include magnetic field sensors, radar technology, antennas, microwave sensors and components, and electromagnetic scattering in disperse media.

Muthuraman Muthuraman was born in Chennai, India, in 1980. He received the B.E. degree in electronics and communication engineering from the University of Madras, Madras, India, in 2002, the M.S. degree in digital communications from Christian Albrecht's University, Kiel, Germany, in 2006, and the Ph.D. degree in biomedical engineering from the Technical Faculty, Department of Neurology, Christian Albrecht's University, Kiel, in 2010.

In 2010, he joined the Department of Neurology, University of Kiel, as a Post-Doctoral Researcher, where he became a Senior Post-Doctoral Researcher, in 2013. Since December 2016, he has been with the Department of Neurology, Johannes Gutenberg University Mainz, Mainz, Germany, where he is an Assistant Professor, and the Head of the Department Biomedical Statistics and Multimodal Signal Processing Unit. His current research interests include mathematical methods for time series analysis and source analysis on oscillatory signals, function of oscillatory activity in central motor systems, biomedical statistics, connectivity analyses, multimodal signal processing and analyses of EEG, MEG, fMRI and EMG, structural and network analyses on anatomical MRI and DTI, functional network analyses on PET imaging, machine learning and deep learning, network analyses on proteomic and genomic data.

Günther Deuschl received the M.D. degree from the University of Munich, Munich, Germany.

From 1981 to 1982, he trained at the Department of Neurology, Universities in Munich, and subsequently, in Freiburg, where he was promoted to an Assistant Professor in 1988. In 1991, he spent a sabbatical with the National Institutes of Health, Bethesda, MA, USA. In 1995, he was elected as a Full Professor of neurology with Christian Albrecht's University, Kiel, Germany, and a Chairman of the Department of Neurology, where he is currently a Senior Professor. His current research interests include clinical features and treatment of movement disorders, Parkinson's disease, essential and other tremors and deep Brain Stimulation. A special interest covers clinical studies on deep brain stimulation for Parkinson's disease and the pathophysiology of movement disorders. He has conducted many clinical studies (DBS and drug treatment of Parkinson's diease and tremor) as a PI.

Michael Höft (M'04–SM'08) received the Dipl.-Ing. degree in electrical engineering and the Dr.-Ing. degree from the Hamburg University of Technology, Hamburg, Germany, in 1997 and 2002, respectively.

From 2002 to 2013, he was with the Communications Laboratory, European Technology Center, Panasonic Industrial Devices Europe GmbH, LÃ¼neburg, Germany. There, he was a Research Engineer and a Team Leader, where he was involved in the research and development of microwave circuitry and components, particularly filters for cellular radio communications. From 2010 to 2013, he was also a Group Leader for the research and development of sensor and network devices. Since 2013, he has been a Full Professor with the Faculty of Engineering, Kiel University, Kiel, Germany, where he is currently the Head of the Chair for microwave engineering with the Institute of Electrical and Information Engineering. His current research interests include active and passive microwave components, submillimeter-wave quasi-optical techniques and circuitry, microwave and field measurement techniques, microwave filters, microwave sensors, and magnetic field sensors and related applications.

Dr. Höft is a member of the European Microwave Association, the Association of German Engineers, and the German Institute of Electrical Engineers.